Editors' Suggestion

Exactly solvable models hosting altermagnetic quantum spin liquids

João Augusto Sobral [1], Pietro M. Bonetti [2], Subrata Mandal [1] and Mathias S. Scheurer [1]
[1] *Institute for Theoretical Physics III, University of Stuttgart, 70550 Stuttgart, Germany*
[2] *Department of Physics, Harvard University, Cambridge, Massachusetts 02138, USA*

(Received 3 January 2026; revised 15 July 2026; accepted 9 October 2026; published 28 October 2026)

We construct spin-$\frac{3}{2}$ and spin-$\frac{7}{2}$ models on the square-octagon and checkerboard lattices that are exactly solvable with Majorana representations. They give rise to spin-liquid phases with full spin-rotation and lattice-translational symmetries but broken time-reversal symmetry. Although nonzero on elementary plaquettes, the net orbital magnetic moment is guaranteed to vanish as a result of point symmetries; due to the analogy to long-range ordered altermagnets, these types of phases were dubbed altermagnetic spin liquids in [Sobral *et al.*, Phys. Rev. Res. **7**, 023152 (2025)]. For the spin-$\frac{3}{2}$ model, we find that a g-wave altermagnetic spin liquid emerges as the unique ground state. In contrast, the spin-$\frac{7}{2}$ model exhibits a significantly richer phase diagram, involving different types of chiral spin liquids competing with a d-wave altermagnetic spin liquid. Finally, we identify and characterize the topological and nontopological excitations, illustrating the rich physics of altermagnetic spin liquids resulting from the interplay of nontrivial topological and symmetry aspects of this novel phase of matter.

DOI: 10.1103/ggbl-t6d7

I. INTRODUCTION

Altermagnetism refers to a class of magnetic states with vanishing net magnetization (unlike ferromagnets) which is enforced not as a result of translational symmetry combined with time reversal (like in antiferromagnets) but follows from a combination of the latter with a point-group operation [1]. Although initially driven by their relevance to spintronics, altermagnets have also become subject of intense research in the field of strongly correlated physics and superconductivity [2,3]. For instance, the fate of these long-range ordered altermagnetic phases in regimes dominated by strong quantum fluctuations, particularly in proximity to, or within, quantum spin liquids (QSLs) [4,5], has been recently explored in distinct scenarios [6–8].

Reference [6] showed that a variety of exotic QSLs can descend from long-range ordered parent altermagnets, with some retaining the same (alter)magnetic point-group symmetries in experimentally accessible observables, in both metallic and insulating regimes. Notably, the electronic spectral functions of the doped system can still exhibit the characteristic altermagnetic momentum-dependent splitting, even though the topologically ordered phase maintains full SU(2) spin-rotational invariance. Among the identified phases, the "orbital altermagnet" (see also [9–12] for a discussion of orbital altermagnetism in different contexts) exhibits a pattern of orbital currents arranged in an altermagnetic fashion. The descendant QSL inherits a corresponding structure in its emergent gauge-flux configuration and scalar spin chiralities, leading to its designation as an orbital altermagnetic quantum spin liquid (OAMSL).

Starting from a Kitaev-type [13] gapless $\mathbb{Z}_2$ QSL defined on a bilayer square-octagon lattice, Ref. [7] showed that increasing the strength of additional interactions that commute with both intralayer and interlayer flux operators of the original model drives a first-order transition into a $\boldsymbol{q} = 0$ ordered state. In this phase, a finite local symmetry-breaking order parameter coexists with remnant global $\mathbb{Z}_2$ topological order inherited from the parent gapless QSL, an example of magnetic fragmentation [14–16]. This coexistence motivated the designation of the phase as a $\mathbb{Z}_2$ topological altermagnet. The bands of the fractionalized excitations exhibit a d-wave momentum-dependent spin splitting protected by the combination of a diagonal mirror symmetry and time reversal.

A related phenomenon was identified in an exactly solvable $\mathbb{Z}_2$ quantum-spin(-orbital) liquid on the square lattice [8]. Small perturbations (compared to the flux gap) which obey altermagnetic projective symmetry requirements, and that do not break the integrability of the model, lead to an effective low-energy theory for fermionic partons whose particle-hole asymmetry generates momentum-dependent band splittings that are analogous to altermagnets. These were dubbed fractionalized altermagnets, akin to fractionalized antiferromagnets [17–19], and were classified according to their projective symmetry group [20].

Taken together, these advances reveal that altermagnetic symmetry breaking can appear in QSLs either as a descendant of an ordered parent phase with fully preserved spin-rotation symmetry and potentially additional altermagnetic scalar spin chiralities [6] or through coexistence of an altermagnetic spin texture with remnant $\mathbb{Z}_2$ topological order [7,8].

Motivated by these developments, and building on the Kitaev [13] and Yao-Kivelson [21] constructions, we introduce two exactly solvable models that intrinsically host OAMSLs

Published by the American Physical Society under the terms of the Creative Commons Attribution 4.0 International license. Further distribution of this work must maintain attribution to the author(s) and the published article's title, journal citation, and DOI.

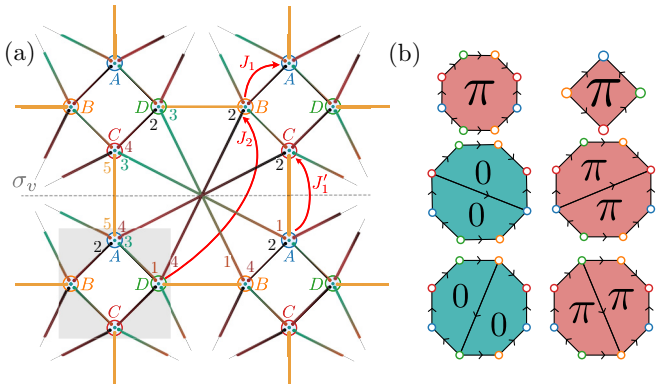


FIG. 1. Schematic representation of the spin-$\frac{3}{2}$ model defined in Eqs. (1) and (5). (a) The chosen unit cell is illustrated with a gray square. The horizontal gray line indicates the σ_v reflection plane. The blue, orange, red, and green circles denote lattice sites belonging to the A, B, C, and D sublattices, respectively. The red arrows denote a particular instance of the interactions with coefficients J_1, J_2, and J_5. The numbers around each lattice site indicate which Γ matrix appears for the given sublattice site in the interaction term along the bond on which the number is located. (b) Gauge flux structure of the g-wave OAMSL. The elementary plaquettes include one square, one octagon, and pentagons inside the latter, with fluxes 0, π, and π, respectively. The arrows indicate the direction in which the respective $\hat{u}_{i_1,i_2}^{\mu_1,\mu_2}$ is positive.

in the sense defined in Ref. [6]. The ground state of the spin-$\frac{3}{2}$ model is a g-wave OAMSL, in sharp contrast with the more complex phase diagram arising for the spin-$\frac{7}{2}$ model. We further address the different types of excitations in the flux sector.

II. SPIN-$\frac{3}{2}$ MODEL

As already outlined above, our goal is to construct an exactly solvable model hosting an OAMSL, which is characterized by the following properties: while spin-rotation invariance is preserved, time-reversal symmetry is spontaneously broken. However, as opposed to a chiral spin liquid (which can be thought of as the ferromagnetic analog of the OAMSL), there are still residual magnetic point-group symmetries that guarantee that the associated net (orbital) magnetic moment vanishes. Similarly to the difference between an antiferromagnet and an altermagnet, we emphasize that the vanishing of the moment is *not* the consequence of the product of time reversal and translation; the OAMSLs we will discuss here all preserve the translational symmetry of the underlying lattice.

In the spirit of the Kitaev [13] and Yao-Kivelson [21] constructions, the coordination number of the lattice determines the "length" S of the spin operators on every site. Furthermore, to break time-reversal symmetry, we require elementary loops with an odd number of sites [22,23]. Focusing on tetragonal two-dimensional systems, as in Ref. [6], the checkerboard lattice seems like a natural starting point to ensure the second constraint. However, the coordination number is six, which requires $S = \frac{7}{2}$. While we will discuss such a model in Sec. III below, we will first reduce the coordination number to five by working on the square-octagon lattice [see Fig. 1(a)]. In this case, $S = \frac{3}{2}$ suffices as its four-dimensional onsite Hilbert space allows for five Γ^a matrices which obey the Clifford algebra $\{\Gamma^a, \Gamma^b\} = 2\delta^{ab}\mathbb{I}_4$. The Hamiltonian is defined by

$$\begin{aligned}\mathcal{H}_{3/2} = \sum_{\boldsymbol{R}} \big[& J_1\big(\Gamma^3_{\boldsymbol{R},A}\Gamma^1_{\boldsymbol{R},D} + \Gamma^4_{\boldsymbol{R},B}\Gamma^2_{\boldsymbol{R},A} + \Gamma^2_{\boldsymbol{R},D}\Gamma^4_{\boldsymbol{R},C} \\ & + \Gamma^1_{\boldsymbol{R},C}\Gamma^3_{\boldsymbol{R},B}\big) + J_1'\big(\Gamma^5_{\boldsymbol{R},D}\Gamma^5_{\boldsymbol{R}_x,B} + \Gamma^5_{\boldsymbol{R}_y,C}\Gamma^5_{\boldsymbol{R},A}\big)\big] + \\ & + \sum_{\boldsymbol{R}} J_2\big(\Gamma^3_{\boldsymbol{R}_y,C}\Gamma^1_{\boldsymbol{R}_x,A} + \Gamma^4_{\boldsymbol{R},A}\Gamma^2_{\boldsymbol{R}_{x+y},C} \\ & + \Gamma^4_{\boldsymbol{R},D}\Gamma^2_{\boldsymbol{R}_{x+y},B} + \Gamma^1_{\boldsymbol{R}_x,B}\Gamma^3_{\boldsymbol{R}_y,D}\big), \end{aligned} \tag{1}$$

with nearest-neighbor couplings J_1 along the edges of the square $\diamondsuit$, J_1' along the horizontal and vertical edges of the octagon $\bigcirc$, and second-neighbor interactions J_2 inside the octagons. Here, $\boldsymbol{R}$ labels the Bravais lattice sites [gray square in Fig. 1(a)] and the shorthands $\boldsymbol{R}_\delta := \boldsymbol{R} + \boldsymbol{e}_\delta$, $\delta = x, y$, and $\boldsymbol{R}_{x+y} := \boldsymbol{R} + \boldsymbol{e}_x + \boldsymbol{e}_y$ are used to refer to neighboring unit cells. The second subscript of the Γ matrices refers to the four sublattices $\alpha = A, B, C, D$ in each unit cell.

There are many different ways of representing the Γ^a matrices acting on the four-dimensional Hilbert space on each site (suppressing the site index here). For instance, they can be expressed in terms of two spin-$\frac{1}{2}$ or two qubits per site. Denoting the Pauli matrices by σ^j, one possible representation is given by

$$\begin{aligned} &\Gamma^1 = \sigma^z \otimes \sigma^y, \quad \Gamma^2 = \sigma^z \otimes \sigma^x, \quad \Gamma^3 = \sigma^y \otimes \mathbb{I}_2, \\ &\Gamma^4 = \sigma^x \otimes \mathbb{I}_2, \quad \Gamma^5 = \sigma^z \otimes \sigma^z. \end{aligned} \tag{2}$$

Alternatively, the Γ^a matrices can also be expressed as spin-$\frac{3}{2}$ operators S^j (see Appendix B), such that Eq. (1) can be reinterpreted as a Hamiltonian with interacting quadrupole moments [24,25].

The point group of the lattice is C_{4v}, which is generated by 90° anticlockwise rotations (C_{4z}) and reflections about the x axis (σ_v), as indicated in Fig. 1(a). From Eq. (1), the symmetry operations act on the Γ^a matrices as follows:

$$\begin{aligned} &C_{4z} : (\Gamma^1, \Gamma^2, \Gamma^3, \Gamma^4) \mapsto (\Gamma^2, \Gamma^3, \Gamma^4, \Gamma^1), \ \Gamma^5 \mapsto -\Gamma^5, \\ &\sigma_v : \Gamma^1 \leftrightarrow \Gamma^2, \ \Gamma^3 \leftrightarrow \Gamma^4, \ \Gamma^5 \leftrightarrow \Gamma^5. \end{aligned} \tag{3}$$

Noting that the Hamiltonian in Eq. (1) remains invariant under both symmetry operations, and we can conclude that its point group is C_{4v}. Furthermore, time reversal is represented by the antiunitary operator Θ with action $\Theta\Gamma^j\Theta^\dagger = \Gamma^j$. In the representation stated in Eq. (2), it is given by $\Theta = \sigma^x \otimes \sigma^y\mathcal{K}$, where $\mathcal{K}$ is the complex-conjugation operator. It is clearly also a symmetry of $\mathcal{H}_{3/2}$ in Eq. (1).

To diagonalize the Hamiltonian (1), we employ a standard Majorana decomposition of the Γ^a matrices, introducing six Majorana fermions per site [shown as colored dots in Fig. 1(a)]. At each site $i = (\boldsymbol{R}, \alpha)$, we define operators c_i^μ and d_i satisfying $\Gamma_i^\mu = i\, c_i^\mu d_i$ ($\mu = 1, \ldots, 5$).

As in the Kitaev model [13], the c_i^μ Majoranas are immobile and generate a static $\mathbb{Z}_2$ gauge-field background through the bond variables $\hat{u}_{i_1,i_2}^{\mu_1,\mu_2} = ic_{i_1}^{\mu_1}c_{i_2}^{\mu_2}$. The mobile d_i Majoranas then form the dispersive bands. Each Majorana fermion contributes a nominal dimension of $\sqrt{2}$ such that the six Majoranas span an enlarged eight-dimensional Fock space,

in contrast to the four-dimensional Hilbert space of a spin $\frac{3}{2}$. Since $\Gamma_i^1\Gamma_i^2\Gamma_i^3\Gamma_i^4\Gamma_i^5 = -\mathbb{I}_4$, $\forall\, i$, all allowed physical states $|\Psi\rangle$ must satisfy a local parity constraint given by

$$D_i^{(3/2)}|\Psi\rangle \equiv \left[-ic_i^1c_i^2c_i^3c_i^4c_i^5d_i\right]|\Psi\rangle = |\Psi\rangle. \tag{4}$$

In practice, this needs to be enforced by the projection operator $|\Psi\rangle = P^{(3/2)}|\psi\rangle \equiv \prod_i[(1+D_i^{(3/2)})/2]|\psi\rangle$, which ensures $D_i^{(3/2)}|\Psi\rangle = |\Psi\rangle$ for all sites. Explicitly, $P^{(3/2)} = [1+\sum_i D_i^{(3/2)} + \sum_{i_1<i_2} D_{i_1}^{(3/2)}D_{i_2}^{(3/2)} + \cdots + \prod_i D_i^{(3/2)}]/2^N$, where N is the total number of sites [21]. The constraint (4) can be naturally rewritten in terms of the $\mathbb{Z}_2$ link variables $u_{i_1,i_2}^{\mu_1,\mu_2}$ and ultimately depends on the lattice boundary conditions (see Appendix A for further details) [26,27].

After rewriting in terms of the Majorana fermions as outlined above, the Hamiltonian then takes the form

$$\begin{aligned}\mathcal{H}_{3/2} = i\sum_{\boldsymbol{R}}\Bigg(&J_1\sum_{(\alpha,\beta,\mu,\nu)\in\mathcal{P}_{\text{intra}}}\hat{u}^{\mu\nu}_{(\boldsymbol{R},\alpha),(\boldsymbol{R},\beta)}d_{\boldsymbol{R},\alpha}d_{\boldsymbol{R},\beta}\\ &+J_1'\sum_{(\delta_1,\delta_2,\alpha,\beta)\in\mathcal{P}'}\hat{u}^{55}_{(\boldsymbol{R}_{\delta_1},\alpha),(\boldsymbol{R}_{\delta_2},\beta)}d_{\boldsymbol{R}_{\delta_1},\alpha}d_{\boldsymbol{R}_{\delta_2},\beta}\Bigg)\\ &+i\sum_{\boldsymbol{R}}J_2\sum_{(\delta_1,\delta_2,\alpha,\beta,\mu,\nu)\in\mathcal{P}_{\text{inter}}}\hat{u}^{\mu\nu}_{(\boldsymbol{R}_{\delta_1},\alpha),(\boldsymbol{R}_{\delta_2},\beta)}d_{\boldsymbol{R}_{\delta_1},\alpha}d_{\boldsymbol{R}_{\delta_2},\beta}\\ &+\text{H.c.},\end{aligned} \tag{5}$$

with $\mathcal{P}_{\text{intra}}$, $\mathcal{P}'$, and $\mathcal{P}_{\text{inter}}$ denoting the sets of intra-unit-cell, primed, and inter-unit-cell bonds, respectively, defined as [see Fig. 1(a)]

$$\begin{aligned}\mathcal{P}_{\text{intra}} &= \{(A,D,3,1),(B,A,4,2),(C,B,2,4),(D,C,1,3)\},\\ \mathcal{P}' &= \{(0,x,D,B),(y,0,C,A)\},\\ \mathcal{P}_{\text{inter}} &= \{(y,x,C,A,3,1),(0,x+y,A,C,4,2),\\ &\qquad (0,x+y,D,B,4,2),(x,y,B,D,1,3)\}.\end{aligned} \tag{6}$$

From their definition, the Hermitian bond operators $\hat{u}_{i_1,i_2}^{\mu_1,\mu_2}$ satisfy $(\hat{u}_{i_1,i_2}^{\mu_1,\mu_2})^2 = 1$ and commute with the Hamiltonian, so they are conserved quantities with eigenvalues ±1. Thus, Eq. (5) describes free Majorana fermions d_i moving in a static $\mathbb{Z}_2$ gauge-field background specified by the eigenvalues of $\{\hat{u}_{i_1,i_2}\}$. Since the $\{\hat{u}_{i_1,i_2}\}$ are not gauge invariant, we instead focus on closed loops of them, which define conserved and gauge-invariant fluxes through the areas they enclose. As they serve as building blocks of fluxes through larger areas, we here focus on the fluxes through the elementary plaquettes (squares, octagons, and pentagons inside the latter) via the Wilson loop operators $\hat{W}_{\text{EP}} = \prod_{\langle ij\rangle\in\text{EP}}\hat{u}_{ij}$, where $\text{EP} \in \{\hexagon, \diamond, \pentagon, \pentagon, \pentagon, \pentagon, \pentagon, \pentagon, \pentagon, \pentagon\}$. Throughout this work, we will follow the conventions that those loops are taken in a clockwise orientation.

For finite couplings $|J_{\{1,1',2\}}| \leqslant 20$, we find numerically that the ground state has π fluxes on the square and octagon plaquettes, with a staggered orbital flux pattern on the eight pentagons, as summarized graphically in Fig. 1(b). This can be contrasted with the square-octagon monolayer limit in Ref. [7], where a ground state with uniform π fluxes on the squares and octagons is found, which is a consequence of Lieb's theorem [28]. Importantly, they consider a distinct model from Eq. (1) with no analog of our J_2 couplings, which is essential to bipartiteness.

Importantly, as a result of the antiunitary nature of time reversal, it must hold $\Theta c_i^\mu \Theta^\dagger = c_i^\mu$ and $\Theta d_i \Theta^\dagger = -d_i$ (modulo any additional $\mathbb{Z}_2$ gauge transformation, irrelevant for our discussion here). This further implies that $\Theta\hat{u}_{i_1,i_2}^{\mu_1,\mu_2}\Theta^\dagger = -\hat{u}_{i_1,i_2}^{\mu_1,\mu_2}$ and, hence, all Wilson loop operators with an even and odd number of edges are even and odd under time reversal, respectively. Consequently, the flux configuration in Fig. 1(b) with 0 and π swapped in the eight pentagons is degenerate with the one shown. Favoring one over the other in the ground state will spontaneously break time-reversal symmetry. Further inspection of the flux pattern reveals that it preserves σ_v and C_{4z}; these symmetries ensure that the net magnetization vanishes and the associated time-reversal-odd altermagnetic order parameter transforms under A_1 of C_{4v}. Since the lowest-order contribution in a multipole expansion of the magnetization is of the form $xy(x^2-y^2)$, one can think of it as a g-wave altermagnet [1,29,30]. Recalling that spin-rotation invariance is preserved in the QSL ground state and this form of time-reversal symmetry breaking is in the orbital channel, we refer to it as a g-wave OAMSL. In Appendix C, we demonstrate that these symmetries' properties are also directly visible in the Berry curvature.

III. SPIN-$\frac{7}{2}$ MODEL

As already anticipated above, we next continue with a model on the checkerboard lattice [see Fig. 2(a)]. As each site is coupled to six neighbors, we need at least six anticommuting matrices. This can be realized with an eight-dimensional irreducible representation of the Clifford algebra, which leads to a total of seven 8×8 matrices γ^a ($a = 1,2\ldots,7$) obeying $\{\gamma^a,\gamma^b\} = 2\delta^{ab}\mathbb{I}_8$. In particular, one possible three-qubit per site (or three spin-$\frac{1}{2}$) representation is given by

$$\begin{aligned}\gamma^1 &= \sigma^x\otimes\sigma^z\otimes\sigma^x,\\ \gamma^2 &= \sigma^x\otimes\sigma^y\otimes\mathbb{I}_2,\\ \gamma^3 &= \sigma^x\otimes\sigma^x\otimes\mathbb{I}_2,\\ \gamma^4 &= \sigma^z\otimes\mathbb{I}_2\otimes\mathbb{I}_2,\\ \gamma^5 &= \sigma^y\otimes\mathbb{I}_2\otimes\mathbb{I}_2,\\ \gamma^6 &= \sigma^x\otimes\sigma^z\otimes\sigma^y,\\ \gamma^7 &= \sigma^x\otimes\sigma^z\otimes\sigma^z.\end{aligned} \tag{7}$$

Instead of just thinking of the local onsite degrees of freedom as some eight-level systems, one can also construct them as polynomials of spin-$\frac{7}{2}$ operators. We refer to Appendix B for details. With one γ matrix more than the number of neighbors, we can also include additional exchange couplings involving the commutators $\gamma^{ab} = [\gamma^a,\gamma^b]/2i$, without spoiling the exact solvability of the model in terms of Majorana fermions.

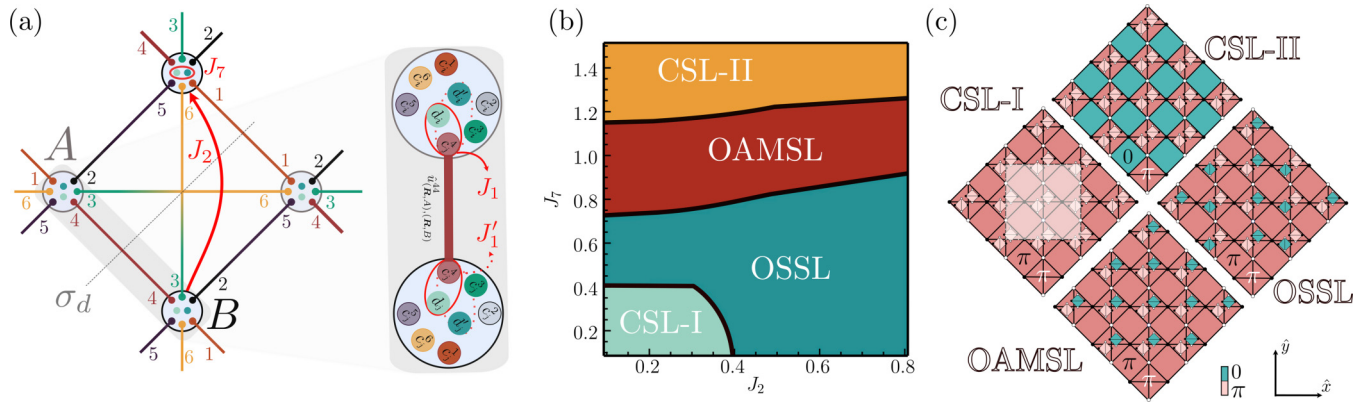


FIG. 2. Schematic representation of the spin-$\frac{7}{2}$ model in Eqs. (1) and (5). (a) Lattice structure with the σ_d reflection symmetry indicated by the diagonal dashed gray line. As in Fig. 1(a), the numbers around each lattice site indicate which γ^a matrix appears in the interaction term for the given sublattice site along the corresponding bond. Each colored dot represents one Majorana fermion, as defined in Eq. (10) and also shown in the zoomed-in unit cell. The red lines and symbols illustrate representative interactions with coefficients J_1, J_2, and J_7. (b) Phase diagram as a function of J_2 and J_7 for $J_2' = J_2$ and $J_1' = J_1 = 1$. In this regime, there are two chiral spin liquids (CSL), an orbital altermagnetic spin liquid (OAMSL), and an orbital stripy spin liquid (see main text for further details about each phase). (c) Flux configurations for each phase shown in (b). Elementary plaquettes (empty and crossed squares, and triangles inside the latter) are colored according to their gauge flux (oriented clockwise), with values 0 (green) or π (red). The white square in the CSL-I phase indicates the unit-cell size considered in our analysis.

The explicit Hamiltonian we study is defined as

$$\begin{aligned}\mathcal{H}_{7/2} = \sum_{\boldsymbol{R}} \big[& J_1\big(\gamma^4_{\boldsymbol{R},A}\gamma^4_{\boldsymbol{R},B} + \gamma^2_{\boldsymbol{R},A}\gamma^5_{\boldsymbol{R}_y,B} + \gamma^1_{\boldsymbol{R}_x,A}\gamma^1_{\boldsymbol{R}_y,B} \\ & + \gamma^2_{\boldsymbol{R},B}\gamma^5_{\boldsymbol{R}_x,A}\big) + J_2\big(\gamma^3_{\boldsymbol{R},A}\gamma^6_{\boldsymbol{R}_x,A} + \gamma^3_{\boldsymbol{R},B}\gamma^6_{\boldsymbol{R}_y,B}\big) \\ & - J_7\big(\gamma^7_{\boldsymbol{R},A} + \gamma^7_{\boldsymbol{R},B}\big)\big] \\ & + \sum_{\boldsymbol{R}} \big[J_1'\big(\gamma^{47}_{\boldsymbol{R},A}\gamma^{47}_{\boldsymbol{R},B} + \gamma^{27}_{\boldsymbol{R},B}\gamma^{57}_{\boldsymbol{R}_y,B} + \gamma^{17}_{\boldsymbol{R}_x,A}\gamma^{17}_{\boldsymbol{R}_y,B} \\ & + \gamma^{27}_{\boldsymbol{R},B}\gamma^{57}_{\boldsymbol{R}_x,A}\big) + J_2'\big(\gamma^{37}_{\boldsymbol{R},B}\gamma^{67}_{\boldsymbol{R}_y,B} + \gamma^{37}_{\boldsymbol{R},A}\gamma^{67}_{\boldsymbol{R}_x,A}\big)\big], \end{aligned} \tag{8}$$

with first-neighbor interactions (J_1, J_1') on the diagonal sides of the squares $\diamondsuit$, diagonal (J_2, J_2') couplings on the crossed squares $\boxplus$, and onsite J_7 couplings. We use the same notation as above with $\boldsymbol{R}$ labeling the Bravais lattice sites, the shorthand $\boldsymbol{R}_{x,y} := \boldsymbol{R} + \boldsymbol{e}_{x,y}$, and the second subscript referring to the two sublattices $\alpha = A, B$ in each unit cell. As we will see below, the primed exchange couplings $J_{1,2}'$ are necessary to make the model sufficiently generic and to remove an extensive degeneracy, and J_7 will be instrumental in stabilizing nontrivial orbital textures over triangle fluxes.

If we demand that the representations of the transformations in the 8×8 space of the γ^a are site independent, this model will have fewer symmetries than the previous one. In that case, the point group is now C_{2v}, which is generated by 180° anticlockwise rotations (C_{2z}) and reflections about the diagonal axis (σ_d) indicated in Fig. 2(a). The symmetry operations act on the γ^a matrices as

$$\begin{aligned} & C_{2z} : \gamma^1 \mapsto -\gamma^4,\ \gamma^4 \mapsto \gamma^1,\ (\gamma^2, \gamma^3) \leftrightarrow (\gamma^5, \gamma^6),\ \gamma^7 \mapsto \gamma^7, \\ & \sigma_d : \gamma^j \to \gamma^j\ (j = 1, \ldots, 7). \end{aligned} \tag{9}$$

Although the lattice also has a σ_v symmetry and a 90° rotational symmetry C_{4z}, these are not compatible with placing the γ^a on the bonds and site-independent representations: the exact solvability requires that the indices a of the γ^a matrices "meeting" at any vertex must all be different. Applying this to the vertex B in Fig. 2(a), we conclude that three disjoint pairs of the seven γ matrices must swap under σ_v (for instance, $\gamma^1 \leftrightarrow \gamma^2$, $\gamma^3 \leftrightarrow \gamma^6$, $\gamma^4 \leftrightarrow \gamma^5$). However, applying it to the vertex A also requires that at least two γ matrices must map to themselves under σ_v, leading to a contradiction. Since σ_v would follow from σ_d and C_{4z}, it cannot be possible to realize C_{4z} either. We note, however, that there is a site-dependent representation, i.e., $\gamma_i^a \to U_g(i)\gamma_{gi}^a U_g^\dagger(i)$ of the symmetries $g = C_{4z}, \sigma_v$ leaving the Hamiltonian (8) invariant (see Appendix B). Although not essential for the definition of the OAMSL, we will use this below to further characterize the flux patterns of the different spin liquids.

To diagonalize the Hamiltonian (8), we employ another Majorana decomposition given by

$$\gamma_i^a = ic_i^a d_i,\ \ \gamma_i^{a7} = ic_i^a d_i',\ \text{and}\ \gamma_i^7 = id_i' d_i, \tag{10}$$

where $a = 1, \ldots, 6$ and we again used the multi-index notation $i = (\boldsymbol{R}, \alpha)$. These eight Majorana fermions are indicated as colored dots on each site in Fig. 2(a). Although the c_i^μ fermions are still immobile, there are now two mobile d_i and d_i' fermions. The enlarged 16-dimensional Fock space, in contrast to the 8-dimensional Hilbert space of a spin-$\frac{7}{2}$, needs the constraint $D_i^{(7/2)}|\Psi\rangle \equiv [c_i^1 c_i^2 c_i^3 c_i^4 c_i^5 c_i^6 d_i\, d_i']|\Psi\rangle = |\Psi\rangle$, arising from $i\gamma_i^1\gamma_i^2\gamma_i^3\gamma_i^4\gamma_i^5\gamma_i^6\gamma_i^7 = \mathbb{I}_8$ (see Appendix A). By introducing the new bond operators $\hat{u}_{i_1,i_2}^{\mu_1,\mu_2} = ic_{i_1}^{\mu_1} c_{i_2}^{\mu_2}$, the

Hamiltonian in Eq. (8) can be rewritten as

$$\mathcal{H}_{7/2} = i\sum_{\boldsymbol{R}}\left[\sum_{(\delta_1,\delta_2,\alpha,\beta,\mu,\nu)\in\mathcal{P}_{\diamondsuit}} \hat{u}^{\mu\nu}_{(\boldsymbol{R}_{\delta_1},\alpha),(\boldsymbol{R}_{\delta_2},\beta)}\left(J_1 d_{\boldsymbol{R}_{\delta_1},\alpha} d_{\boldsymbol{R}_{\delta_2},\beta} + J_1' d'_{\boldsymbol{R}_{\delta_1},\alpha} d'_{\boldsymbol{R}_{\delta_2},\beta}\right) - J_7\left(d'_{\boldsymbol{R},A} d_{\boldsymbol{R},A} + d'_{\boldsymbol{R},B} d_{\boldsymbol{R},B}\right)\right] + i\sum_{\boldsymbol{R}}\sum_{(\delta_1,\delta_2,\alpha,\beta)\in\mathcal{P}_{\diamondplus}} \hat{u}^{36}_{(\boldsymbol{R}_{\delta_1},\alpha),(\boldsymbol{R}_{\delta_2},\beta)}\left(J_2 d_{\boldsymbol{R}_{\delta_1},\alpha} d_{\boldsymbol{R}_{\delta_2},\beta} + J_2' d'_{\boldsymbol{R}_{\delta_1},\alpha} d'_{\boldsymbol{R}_{\delta_2},\beta}\right) + \text{H.c.}, \tag{11}$$

with $\mathcal{P}_{\diamondsuit}$ and $\mathcal{P}_{\diamondplus}$ denoting the sets of first- and second-neighboring bonds, defined as [see Fig. 2(a)]

$$\begin{aligned}\mathcal{P}_{\diamondsuit} &= \{(0,0,A,B,4,4),(0,y,A,B,2,5),\\ &\quad (x,y,A,B,1,1),(0,x,B,A,2,5)\},\\ \mathcal{P}_{\diamondplus} &= \{(0,x,A,A),(0,y,B,B)\}.\end{aligned} \tag{12}$$

This Hamiltonian describes free $d_{i,\alpha}$ and $d'_{i,\alpha}$ Majorana fermions. In this representation, the difference between the $J_{\{1,2\}}$ and $J'_{\{1,2\}}$ couplings becomes clearer. As is also visualized schematically in the zoomed-in region of Fig. 2(a), the unprimed (primed) couplings couple the $d_{i,\alpha}$ ($d'_{i,\alpha}$) fermions located on different sites. So we see that both of these couplings are required to stabilize a finite bandwidth of both fermion flavors and, thus, to remove an otherwise extensive ground-state degeneracy. Additionally, a finite J_7 coupling hybridizes the two mobile Majorana fermion bands. Upon combining the Majorana fermions $d_{i,\alpha}$ and $d'_{i,\alpha}$ into complex (Abrikosov) fermions, this term maps onto a chemical potential, thereby explicitly breaking particle-hole symmetry.

Once again, the bond operators $\hat{u}^{\mu_1,\mu_2}_{i_1,i_2}$ are constants of motion: each can have an eigenvalue ± 1 and commutes with the Hamiltonian, so they form a static $\mathbb{Z}_2$ gauge field background for the mobile Majorana fermions. The relevant conserved fluxes for the elementary plaquettes (empty and crossed squares, and triangles inside the latter) are given by the Wilson loop operators $\hat{W}_{\text{EP}} = \prod_{\langle ij\rangle\in\text{EP}} \hat{u}_{ij}$, where $\text{EP} \in \{\diamondsuit, \diamondplus, \blacklozenge, \blacklozenge, \blacklozenge, \blacklozenge\}$ and all paths are taken in a clockwise way.

After diagonalizing Eq. (11) numerically in momentum space for all unique flux configurations modulo symmetries, we have found four phases in the phase diagram [Fig. 2(b)] for fixed $J_1 = J_1' = 1$, $|J_2| \leqslant 0.8$, and $|J_7| \leqslant 1.5$. These can be characterized through the six distinct fluxes on the elementary plaquettes $\{\diamondsuit, \diamondplus \mid \blacklozenge, \blacklozenge, \blacklozenge, \blacklozenge\}_{\boldsymbol{R}}$ associated with each unit cell $\boldsymbol{R}$ (see Appendix D for more details). By considering a super unit cell of eight sites, we visually represent the fluxes of these phases in Fig. 2(c).

Starting from finite J_1 and J_1' while $J_2 = J_2' = J_7 = 0$, the ground state exhibits a uniform π flux on the square $\diamondsuit$ plaquettes, consistent with Lieb's theorem [28]. Upon introducing the onsite J_7 couplings, this uniform flux configuration in the square plaquettes persists up to $J_7 \simeq 1.2$. Beyond this threshold, the ground state transitions to a staggered flux pattern with 0 and π fluxes on the $\diamondsuit$ and $\diamondplus$ plaquettes, respectively. The phases that emerge at small J_2 and J_2' can be understood as natural extensions of these two flux configurations, now featuring additional nontrivial orbital textures on the triangular elementary plaquettes.

At small $J_{\{2,7\}}$, we find a state with a uniform flux configuration $\{-,- \mid -,-,-,-\}_{\boldsymbol{R}}$, which preserves the rotational symmetry of the lattice but is odd under σ_d. There is a finite (orbital) magnetic moment in the unit cell and the state represents a chiral spin liquid [denoted by CSL-I in Fig. 2(b)]. Increasing either J_2 or J_7 induces more nontrivial orbital textures over the triangle fluxes. First, we obtain a state where the orbital textures alternate in an antiferromagnetic fashion along one direction [$\hat{x}$ in Fig. 2(c)]; we refer to this state as an orbital stripy spin liquid (OSSL). Most importantly for us here, for larger J_7, we again obtain an OAMSL: as can be seen from the flux configurations depicted in Fig. 2(c), it preserves translations, σ_d, and the combination of time reversal Θ and C_{4z}, while those last two symmetries are broken individually. As such, the associated altermagnetic order parameter transforms under B_2 of C_{4v}; it can, thus, be thought of as a d-wave OAMSL and is very closely related to the state discussed in Ref. [6]. We note for completeness that being even under σ_d is already sufficient to force the magnetization to vanish since the only finite moments are orbital moments, which are Ising type in two spatial dimensions.

Finally, these orbital textures are destroyed upon increasing J_7 further, giving rise to a second chiral spin liquid (CSL-II) with a checkerboard flux pattern between elementary square plaquettes $\{-,+ \mid -,-,-,-\}_{\boldsymbol{R}}$.

By considering $|J_{\{2,7\}}| \geqslant 1.5$, we found an even richer phase diagram with additional phases that can be stabilized, including p-wave OAMSLs, as well as regions of increased degeneracy. Transitions between the distinct phases occur as level crossings of the ground-state energy obtained by comparing the distinct possible gauge configurations, and are generically first order, with the flux pattern changing discontinuously. Apart from CSL-I and CSL-II, all these phases were found to have gapless spinon excitations for the considered couplings $J_{\{2,7\}}$. For the specified configurations, both CSLs are characterized by a Chern number of $C = -2$ (see discussion in Appendix C). We refer the reader to Fig. 7 and Appendix D for more details.

IV. FLUX EXCITATIONS FOR THE OAMSL

Having established the ground-state properties of the spin models, we now examine their flux excitations. Our primary focus is the OAMSL in the spin-$\frac{7}{2}$ model, though this analysis can be readily extended to other phases, including those in the

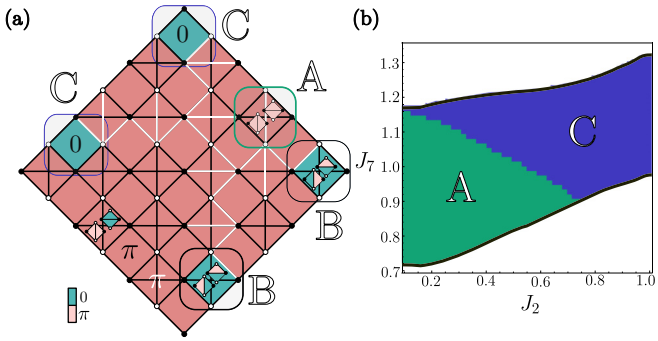


FIG. 3. (a) Schematic representation of flux excitations in the OAMSL phase of the spin-$\frac{7}{2}$ model. The nontopological excitation (A) consists of localized flux flips within a single plaquette, requiring no gauge string for creation or annihilation. Two topological excitations (visons B and C) are shown with their characteristic gauge strings (white); the gauge strings carry zero-energy cost and enable free vison propagation. We indicate the modified flux patterns on triangular plaquettes relative to the staggered ground-state configuration (not shown for clarity). (b) Type of the lowest flux excitation within the OAMSL domain as a function of J_2 and J_7 for $J_2' = J_2$ and $J_1' = J_1 = 1$. See also Fig. 10 for more details.

spin-$\frac{3}{2}$ model. There are three possible elementary excitations in the flux sector: one nontopological (A) and two topological (visons B and C), as illustrated in Fig. 3(a).

The nontopological excitations (A) arise from bond flips within filled squares ✣. These excitations manifest as local ferromagnetic moments, characterized by uniform fluxes inside the elementary triangles of the lattice, i.e., $(+,+,+,+)$ or its time-reversal conjugate $(-,-,-,-)$. This locally breaks σ_d and thus can be thought of as the local creation of a chiral configuration within a single unit cell. Since they can be created within a single filled square and moved without requiring a gauge string, they lack the topological character of visons.

As for the topological excitations, we first consider configurations where empty square fluxes remain fixed, while triangles and filled square ✣ fluxes undergo minimal changes. This corresponds to vison-B excitations with dipolar end points that break the original alternating $(+,-,+,-)$ flux pattern of triangles in the OAMSL. At the string end points, the flux configurations become $(-,-,+,+)$ and $(-,+,+,-)$ configurations leading to local dipolar structures, in contrast to the quadrupolar structure of the underlying OAMSL. The end points can propagate independently at opposite ends of the string but necessarily leave a string of flipped gauge configurations behind, signaling their topological visonlike nature. Moreover, each end point's dipole can independently rotate to $(+,+,-,-)$, $(-,+,+,-)$, $(-,-,+,+)$, or $(+,-,-,+)$. This yields four distinct states per end point. Consequently, these defects carry additional quantum numbers compared to conventional visons in simpler $\mathbb{Z}_2$ spin liquids, a direct consequence of the sublattice structure. These excitations can move freely and constitute genuine topological excitations that, once separated, cannot be annihilated through local operations.

If we also allow the empty square plaquettes to flip, we obtain a second type of vison excitation, labeled by C in Fig. 3(a). They do not break any symmetries and, as opposed to the vison-B excitations, do not carry additional internal quantum numbers.

Figure 3(b) indicates in the parameter regime of the OAMSL which excitation type has the lowest energy. The nontopological excitation A exhibits the smallest gap at low J_2 coupling, while vison C becomes preferred as J_2 increases. Despite vison B appearing to have a larger gap throughout this domain, we note a region in parameter space near $J_7 \simeq 1.1$ at small J_2 values, where all three types of excitations are nearly degenerate (see Fig. 10).

V. CONCLUSION

We have constructed and analyzed two exactly solvable two-dimensional spin models hosting orbital altermagnetic and other competing quantum spin liquids. Although both are defined on tetragonal Bravais lattices, their phase diagrams differ significantly: the first model can be thought of as spin-$\frac{3}{2}$ degrees of freedom (or two qubits) on the sites of a square-octagon lattice [see Fig. 1(a) or Eq. (1)]. Despite the large number of intra-unit-cell degrees of freedom and the fact that the lattice geometry allows for various other orbital textures, we found that a g-wave orbital altermagnetic spin liquid consistently exhibits the lowest ground-state energy in the parameter regime we have considered. The second model we constructed is defined on the checkerboard lattice, which requires three qubits per site (or spin $\frac{7}{2}$) to retain exact solvability via a Majorana representation. As opposed to the spin-$\frac{3}{2}$ model, the phase diagram is rich and features several distinct spin liquids, including chiral spin liquids, translational-symmetry-breaking spin liquids, but also a d-wave altermagnetic spin liquid. We further analyzed the possible excitations in the flux sector, which are summarized graphically in Fig. 3(a) and reveal both topological visonlike excitations that are associated with gauge strings (B and C) as well as nontopological local ferromagnetic flips of the gauge fields (A). These excitations can be accessed experimentally with local probes [31].

In the future, it would be interesting to explore the impact of additional perturbations, such as a static magnetic fields in analogy with the Kitaev model [13] or higher-order interactions [32,33]. Another important future direction would be to analyze how these models and, hence, orbital altermagnetic phases in general, could be stabilized in programmable quantum-simulation platforms, such as Rydberg-atom arrays [34].

ACKNOWLEDGMENTS

The authors thank V. Dantas, R. G. Pereira, S. Chesi, L. Pupim, and S. Banerjee for insightful discussions. S.M. and M.S.S. further acknowledge funding by the European Union (Grant No. ERC-2021-STG, Project No. 101040651—SuperCorr). Views and opinions expressed are, however, those of the authors only and do not necessarily reflect those of the European Union or the European Research Council Executive Agency. Neither the European Union nor the granting

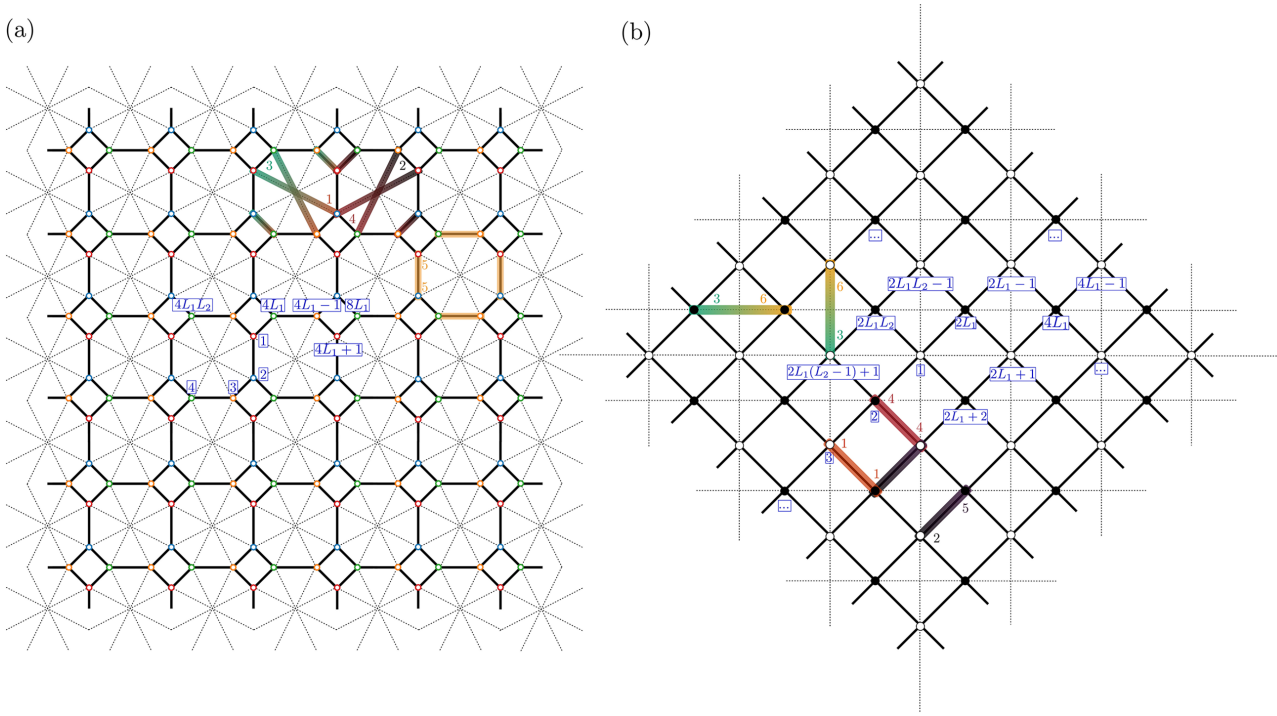


FIG. 4. Boundary conditions for the spin-$\frac{3}{2}$ (a) and spin-$\frac{7}{2}$ models (b). Each site is indicated through blue boxed labels. The representative bonds $\hat{u}_{ij}^{\alpha,\tau}$ for each model are represented and colored in accordance with Figs. 1(a) and 2(a).

authority can be held responsible for them. P.M.B. acknowledges support by the German National Academy of Sciences Leopoldina through Grant No. LPDS 2023-06, by the Gordon and Betty Moore Foundation's EPiQS Initiative Grant No. GBMF8683, and by the NSF Grant No. DMR-2245246.

DATA AVAILABILITY

There are no publicly available research data or software supporting this manuscript. Requests for further information or data should be sent to the authors.

APPENDIX A: LOCAL PHYSICAL CONSTRAINTS FOR MAJORANAS

Kitaev's solution of the honeycomb-lattice model offers a significant simplification by mapping the diagonalization of a $2^{2N} \times 2^{2N}$ Hamiltonian to the problem of diagonalizing $2N \times 2N$ matrix [13]. However, this mapping comes at the expense of enlarging the Hilbert space through the introduction of Majorana fermions; thereby, the resulting eigenstates of the Majorana Hamiltonian may not correspond to physical states of the original spin system. To recover the physical ground state, a projection onto the physical subspace is necessary. This can be enforced by the local gauge constraints $D_i|\psi\rangle = |\psi\rangle$ at each site i. To be more precise, it can be shown that the operators D_i generate the projection operator P, which can be written explicitly as $P = \mathcal{S}P_0$, where $\mathcal{S}$ contains all inequivalent gauge transformations and $P_0 = (1 + D)/2$ with $D \equiv \prod_i D_i$.

1. The projection operator in the square-octagon lattice

This appendix presents the rewriting of the projection operator in the square-octagon lattice in terms of fermion parities and link variables. More specifically, we focus on a square-octagon lattice embedded on a torus, with the labeling shown in Fig. 4(a). We begin with the definition

$$2P_0^{(3/2)} = 1 + D^{(3/2)}, \tag{A1}$$

where the gauge operator is defined as $D^{(3/2)} = \prod_i D_i^{(3/2)} = \prod_i (-i) c_i^1 c_i^2 c_i^3 c_i^4 c_i^5 d_i = \prod_i c_i^1 c_i^2 c_i^3 c_i^4 c_i^5 d_i$. Here, we also assume that the total number of sites in our square-octagonal lattice is $N = 4L_1L_2$.

To reexpress the projection operator in terms of the link operators, first, we bring all c-Majorana operators to the right of the d-Majorana operators. Next, we group the c^1 and c^3 operators together, as well as the c^2 and c^4 operators, so that they can be associated with u operators. When we rearrange the operators, the anticommutation of the Majorana operator produces an overall factor of $(-1)^N$. Since N is even in our case, this phase factor becomes unity, and the regrouping can be carried out without additional sign. This leads us to

$$D^{(3/2)} = \prod_i^N c_i^1 c_i^3 \prod_j^N c_j^2 c_j^4 \prod_k^N c_k^5 d_k. \tag{A2}$$

The remaining product can be further simplified by separating the operators c^5 and d. This can again be done without introducing any phase factor. Thus, operator D decomposes into

the product of four independent pieces, yielding

$$D^{(3/2)} = \prod_i^N c_i^1 c_i^3 \prod_j^N c_j^2 c_j^4 \prod_k^N c_k^5 \prod_l^N d_l. \tag{A3}$$

When we evaluate the first three pieces involving the c operators, they reduce to the product of u operators, accompanied by some additional phase factors that originate from the rearrangement of Majorana operators. After simplification, these products turn out to be

$$\prod_i^N c_i^1 c_i^3 = (-1)^{L_1 L_2} \prod_{ij} u_{ij}^{31}, \tag{A4}$$

$$\prod_i^N c_i^2 c_i^4 = (-1)^{L_1 L_2} \prod_{ij} u_{ij}^{24}, \tag{A5}$$

$$\prod_i^N c_i^5 = (-1)^{L_1 L_2} \prod_{ij} u_{ij}^{55}. \tag{A6}$$

We are now only left with d-Majorana operators. To evaluate the contribution of these d-Majorana operators, it is convenient to introduce complex bond fermions, which are defined as $f_1 = (d_C - id_A)/2$ and $f_2 = (d_B - id_D)/2$. As a result, within this representation, the product over d Majoranas can be expressed as

$$\prod d_i = (-1)^{L_1 L_2} (-1)^{N_\chi}, \tag{A7}$$

where N_χ denotes the number of bond fermions.

This leads directly to the explicit form of the projection operator given by

$$2P_0^{(3/2)} = 1 + (-1)^{N_\chi} \prod u_{ij}^{31} \prod u_{kl}^{55} \prod u_{mn}^{24}. \tag{A8}$$

2. The projection operator in the checkerboard lattice

In this section, we derive the projection operator for the checkerboard lattice, which is embedded on a torus, and adopt the labeling illustrated in Fig. 4(b). We again start from the definition

$$2P_0^{(7/2)} = 1 + D^{(7/2)}, \tag{A9}$$

but with $D^{(7/2)} = \prod_i D_i^{(7/2)} = \prod_i c_i^1 c_i^2 c_i^3 c_i^4 c_i^5 c_i^6 d_i d_i'$ as the gauge operator. Here, we consider the lattice comprises $2L_1L_2$ sites. In the first step, we move all d and d' operators to the left of the c operators, and we reorder the c operators so that c^1 and c^4, c^6 and c^3, and c^2 and c^5 are adjacent. This rearrangement does not generate any sign change, resulting

$$D^{(7/2)} = \prod_i^N c_i^1 c_i^4 \prod_j^N c_j^6 c_j^3 \prod_k^N c_k^2 c_k^5 \prod_m^N d_m d_m'. \tag{A10}$$

At this stage, we separate the c^1 and c^4 operators, which introduces a phase factor. This yields

$$D^{(7/2)} = (-1)^{\theta_1} \prod_{i_1}^N c_{i_1}^1 \prod_{i_2}^N c_{i_2}^4 \prod_j^N c_j^6 c_j^3 \prod_k^N c_k^2 c_k^5 \prod_m^N d_m d_m', \tag{A11}$$

where $\theta_1 = L_1 L_2 (2L_1 L_2 - 1)$. Now we are ready to write the c operators in terms of u operators. This step introduces additional phase factors as before. After all the algebraic manipulation, we arrive at

$$\prod_i^N c_i^6 c_i^3 = (-1)^{\theta_2} (-1)^{L_1 L_2} \prod_{ij} u_{ij}^{63}, \tag{A12}$$

$$\prod_i^N c_i^1 = (-1)^{\theta_3} (i)^{L_1 L_2} \prod_{ij} u_{ij}^{11}, \tag{A13}$$

$$\prod_i^N c_i^4 = (-1)^{\theta_4} (i)^{L_1 L_2} \prod_{ij} u_{ij}^{44}, \tag{A14}$$

$$\prod_i^N c_i^2 c_i^5 = (-1)^{L_1 L_2 + L_2} \prod_{ij} u_{ij}^{52}, \tag{A15}$$

where $\theta_2 = L_2 + L_1 L_2$, $\theta_3 = L_1 + L_1 L_2$, and $\theta_4 = L_1 + L_2 + L_1 L_2$. Now the remaining Majorana degrees of freedom are d and d' at each site. To proceed further, we introduce a complex fermion at each site, defined as $f_i = (d_i - id_i')/2$. The product of d and d' Majorana operators can then be written explicitly:

$$\prod d_i d_i' = (-1)^{L_1 L_2} (-1)^{N_\chi}, \tag{A16}$$

where N_χ counts the number of complex fermions at each site.

Hence, the projection operator takes the form

$$2P_0^{(7/2)} = 1 + (-1)^{L_2} (-1)^{N_\chi} \prod u_{ij}^{11} \prod u_{mn}^{44} \prod u_{pq}^{63} \prod u_{uv}^{52}. \tag{A17}$$

In this section, we derived two projection operators that determine whether a state $|\Psi\rangle$ lies within the physical subspace or outside of it. More importantly, these operators impose a definite fermionic parity, either even or odd, for a state to be physical. The fermionic parity is generally decided by the gauge configuration and the imposed boundary condition. Once the gauge configuration that minimizes the energy is obtained, the occupation of the complex fermionic can always be adjusted so that the resulting state corresponds to the true physical ground state. We would also like to emphasize that the explicit form of the projection operator depends on both the boundary conditions and the choice of labeling [26,27]. They altogether dictate the physicality of the ground state.

APPENDIX B: SYMMETRIES, CLIFFORD GENERATORS, AND IRREDUCIBLE REPRESENTATIONS OF SU(2)

1. Representation of symmetries

The specific representations for the symmetry operators that transform the Clifford generators in Eqs. (2) and (7) according to Eqs. (3) and (9) are given by

$$C_{4z} = U_\pi(4,5) U_\pi(1,2) U_{\pi/2}(1,4) U_{\pi/2}(2,4) U_{\pi/2}(3,4), \tag{B1}$$

$$\sigma_v = U_\pi(2,4) U_{\pi/2}(3,4) U_{\pi/2}(1,2), \tag{B2}$$

$$C_{2z} = \mathcal{U}_{\pi/2}(4,1) \mathcal{U}_{\pi/2}(5,2) \mathcal{U}_\pi(5,7) \mathcal{U}_{\pi/2}(6,3) \mathcal{U}_\pi(6,7), \tag{B3}$$

$$\sigma_d = \mathbb{I}_8, \tag{B4}$$

where the unitaries are defined as $U_\theta = \exp(\frac{\theta}{4}[\Gamma^a, \Gamma^b])$ and $\mathcal{U}_\omega = \exp(\frac{\omega}{4}[\gamma^a, \gamma^b])$. The antiunitary operator Θ that

transforms the Γ^a matrices in Eq. (2) as $\Theta_{3/2}\Gamma^a\Theta_{3/2}^\dagger = \Gamma^a$ is represented as $\Theta_{3/2} = \sigma_x \otimes \sigma_y \mathcal{K}$, where $\mathcal{K}$ stands for complex conjugation.

In contrast for the spin-$\frac{7}{2}$ model, not all γ^a matrices can be even under time reversal. We choose $\Theta_{7/2} = i\sigma_y \otimes \sigma_x \otimes \mathbb{I}_2\mathcal{K}$ such that $\Theta_{7/2}\gamma^a\Theta_{7/2}^\dagger = s_a\gamma^a$ with $s_1 = s_7 = +1$ and $s_2 = s_3 = s_4 = s_5 = s_6 = -1$. This is clearly a symmetry of $\mathcal{H}_{7/2}$ in Eq. (8). Modulo $\mathbb{Z}_2$ gauge transformations, the Majorana particles transform as

$$\Theta_{7/2}d_i\Theta_{7/2}^\dagger = -d_i, \quad \Theta_{7/2}d_i'\Theta_{7/2}^\dagger = d_i',$$
$$\Theta_{7/2}c_i^a\Theta_{7/2}^\dagger = s_a c_i^a, \tag{B5}$$

which is consistent with the behavior of Eq. (10) under time reversal. Consequently, the link variables transform as $\hat{u}_{i_1,i_2}^{a_1,a_2} = ic_{i_1}^{a_1}c_{i_2}^{a_2} \to -s_{a_1}s_{a_2}\hat{u}_{i_1,i_2}^{a_1,a_2}$. However, note that only the combinations $(a_1, a_2) \in \{(1,1),(4,4),(2,5),(3,6)\}$ matter [cf. Fig. 2(a)], for which $s_{a_1}s_{a_2} = 1$. Consequently, we effectively again obtain $\hat{u}_{i_1,i_2}^{a_1,a_2} \to -\hat{u}_{i_1,i_2}^{a_1,a_2}$ under time reversal, just like in the spin-$\frac{3}{2}$ model.

Finally, we point out that σ_v can be represented in a sublattice-dependent way. Equation (8) stays invariant under σ_v if

$$\text{sublattice A:} \quad (\gamma^1,\gamma^2) \leftrightarrow (\gamma^5,\gamma^4),\ \gamma_{3,6,7} \mapsto \gamma_{3,6,7}, \tag{B6a}$$
$$\text{sublattice B:} \quad (\gamma^1,\gamma^3) \leftrightarrow (\gamma^2,\gamma^6),\ \gamma_4 \mapsto -\gamma_5,\ \gamma_5 \mapsto \gamma_4,\ \gamma_7 \mapsto \gamma_7. \tag{B6b}$$

The associated unitary operators read as

$$\text{sublattice A:} \quad \sigma_v = \mathcal{U}_{\pi/2}(4,2)\mathcal{U}_\pi(4,7)\mathcal{U}_{\pi/2}(5,1)\mathcal{U}_\pi(5,7), \tag{B7a}$$
$$\text{sublattice B:} \quad \sigma_v = \gamma^4\mathcal{U}_{\pi/2}(1,2)\mathcal{U}_\pi(2,7)\mathcal{U}_{\pi/2}(4,5)\mathcal{U}_\pi(5,7)\mathcal{U}_{\pi/2}(3,6)\mathcal{U}_\pi(6,7), \tag{B7b}$$

respectively. Note that C_{4z} follows from σ_d and σ_v.

2. Relation to spin-S operators

As explained in the main text, the Clifford generators can also be represented in terms of spin operators. For the first model, Γ^a can be written in terms of spin-$\frac{3}{2}$ operators S^j as [24,25]

$$\Gamma^1 = \frac{1}{\sqrt{3}}\{S^y,S^z\}, \quad \Gamma^2 = \frac{1}{\sqrt{3}}\{S^z,S^x\}, \quad \Gamma^3 = \frac{1}{\sqrt{3}}\{S^x,S^y\},$$
$$\Gamma^4 = \frac{1}{\sqrt{3}}[(S^x)^2 - (S^y)^2], \quad \text{and} \quad \Gamma^5 = (S^z)^2 - \frac{5}{4}\mathbb{I}_4. \tag{B8}$$

For the second model, one can employ a similar construction using spin-$\frac{7}{2}$ operators L^j. In an irreducible spin-j representation, L_z has eigenvalues $m = -j, -j+1, \ldots, j$. The operators

$$P_m(L^z) = \prod_{m' \neq m} \frac{L^z - m'}{m - m'} \tag{B9}$$

are explicit degree-$(2j)$ polynomials in L^z and form a basis for all diagonal matrices in the $|m\rangle$ basis. Additionally, any off-diagonal operator can be obtained by applying powers of L^+ or L^-, e.g., $|m\rangle\langle n| \propto P_m(L_z)(L^+)^{m-n}$. Since $|m\rangle\langle n|$ form a basis for all matrices, any 8×8 matrix, including the Clifford generators γ^a, can be represented as finite-degree polynomials in the spin-$\frac{7}{2}$ operators L^x, L^y, L^z.

APPENDIX C: BERRY CURVATURE AND MAJORANA BAND SPLITTING

In Fig. 5, we show the band structure for the d-wave OAMSL in the spin-$\frac{3}{2}$ model. The degeneracy from the path $\Gamma \to X \to M$ is lifted in the regime $M \to \Gamma$ alongside the formation of four Dirac cones located at $K_1 = \pm(\frac{\pi}{2},\frac{\pi}{2})$ and $K_2 = \pm(-\frac{\pi}{2},\frac{\pi}{2})$. We note that the Majorana splitting here is not physically equivalent to the conventional electronic splitting in metallic altermagnets since the Majorana operators do not carry spin. In Ref. [7], in contrast, since the model is based on a bilayer square-octagon structure, the bands carry an additional layer ℓ index, which plays the role of spin in the momentum-dependent splitting. A direct analog was discussed in Ref. [6] where doped altermagnetic spin

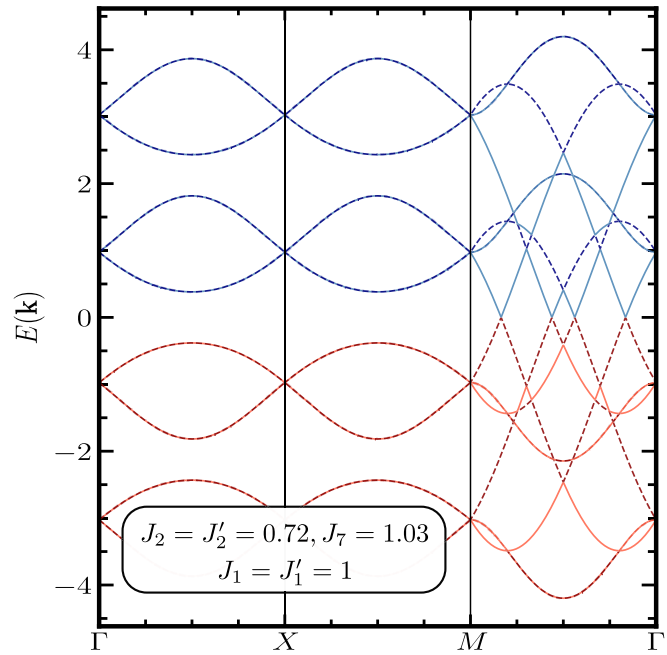


FIG. 5. Majorana band splitting for the d-wave OAMSL in the spin-$\frac{3}{2}$ model for the indicated coupling parameters, and a super unit cell with eight sublattices. Different colors and line styles are used to clearly distinguish between bands.

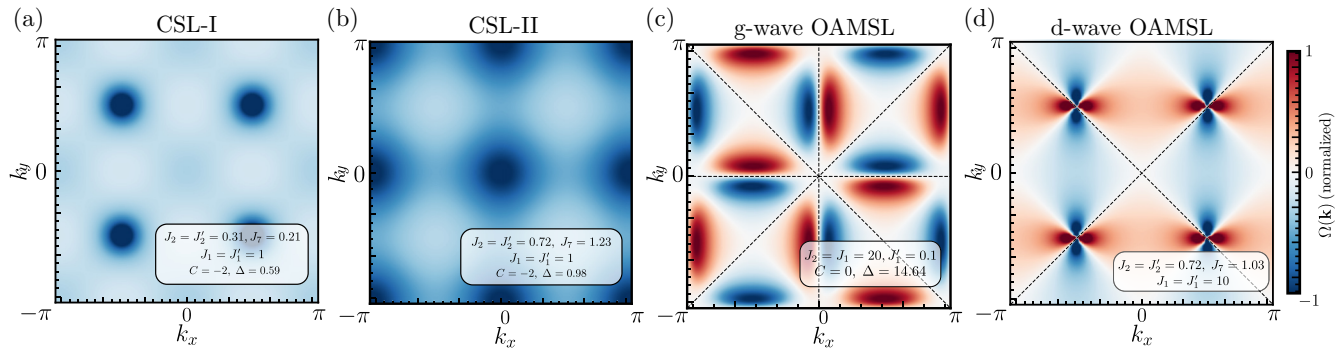


FIG. 6. Normalized Berry curvature $\Omega(\mathbf{k})$ in the Brillouin zone for chiral spin liquids CSL-I (a) and CSL-II (b), and orbital angular momentum spin liquids (OAMSLs) with g-wave (c) and d-wave (d) symmetry. Composite Chern number C and gap size Δ are listed in each panel, along with the corresponding coupling constants. The Chern number and gap size are not shown in (d) as this is a gapless phase. Dashed lines in (c) and (d) mark the sign-changing nodal lines of the Berry curvature.

liquids were considered and found to exhibit a (spin-rotation invariant) electronic spectral function with splittings that are similar to those of the long-range ordered altermagnet.

The nontrivial symmetry structure of our OAMSL is more naturally illustrated from the perspective of the Berry curvature. We start with the g-wave OAMSL for the spin-$\frac{3}{2}$ model. First, we note that for fixed $\{J_1, J_1'\}$ the gap Δ for the phases increases linearly with J_2. The g-wave character is apparent in momentum space, with the presence of lines along $k_x = 0$, $k_y = 0$, $k_x = \pm k_y$ in Fig. 6(c) where the Berry curvature changes its sign.

Turning to the spin-$\frac{7}{2}$ model, although the d-wave OAMSL is gapless around the Dirac points $K_{1,2}$ mentioned above, we can calculate an associated Berry curvature in the vicinity of the nodal points through the Kubo formula

$$\Omega(\mathbf{k}) = -2 \sum_{n\in\text{occ}} \sum_{m\notin\text{occ}} \text{Im} \frac{\langle n\mathbf{k}|\partial_{k_x} H|m\mathbf{k}\rangle\langle m\mathbf{k}|\partial_{k_y} H|n\mathbf{k}\rangle}{(E_m(\mathbf{k}) - E_n(\mathbf{k}))^2 + \eta^2} \tag{C1}$$

with a small Lorentzian broadening that regularizes the gapless denominators (taken here as $\eta = 10^{-4}$). From the associated Berry curvature in Fig. 6(d) we see two nodal lines, as expected from a d-wave character.

APPENDIX D: EXTENDED PHASE DIAGRAM OF THE SPIN-$\frac{7}{2}$ MODEL AND VISON SPECTRUM

In Fig. 7(a), we present the extended phase diagram of the spin-$\frac{7}{2}$ model. As discussed in the main text, increasing J_θ with $\theta = 2, 2', 7$ stabilizes a number of additional phases. These phases are obtained using a super unit cell containing eight sites [indicated by the white square in Fig. 2(c)], and their associated phase-flux configurations are shown in Fig. 8. At $J_2 = J_2' = 0$ and for $J_7 > 2$, the ground state develops a uniform flux configuration, now characterized by a 0 flux through the square $\diamond$ plaquettes. Phases P9 and P10 can be understood as natural extensions of this state, in which additional orbital textures are stabilized by finite values of J_2 and J_2'.

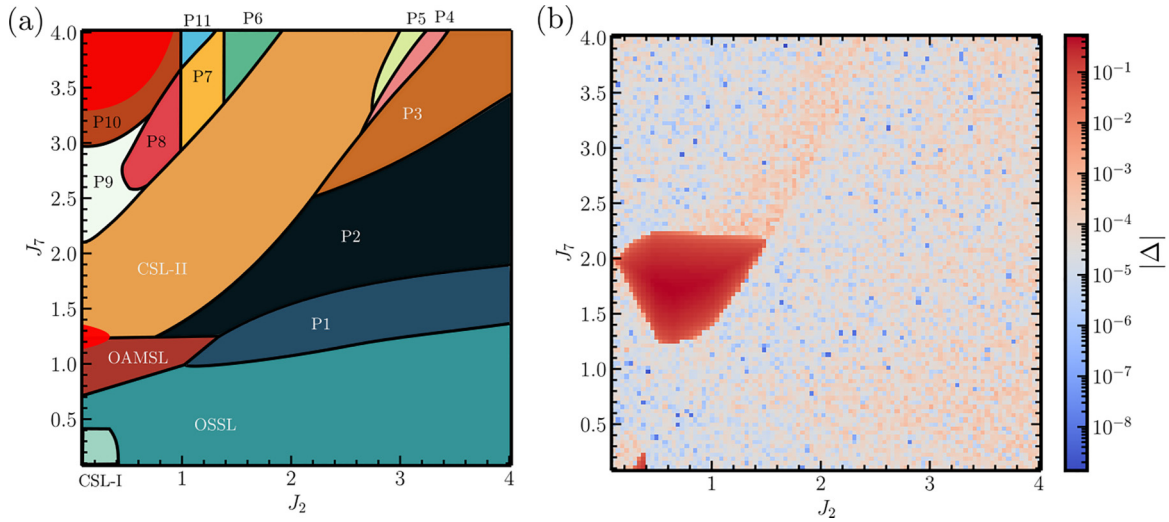


FIG. 7. (a) Extended phase diagram for the spin-$\frac{7}{2}$ model shown in Fig. 2(b). Schematic representations of the flux configurations for each phase P_l ($l = 1, \ldots, 15$) are shown in Fig. 8. (b) Gap Δ (logarithm scale) as a function of the couplings for the phase diagram in (a). As indicated by the color bar, apart from the CSL-I and CSL-II phases, all remaining phases remain gapless over this parameter range.

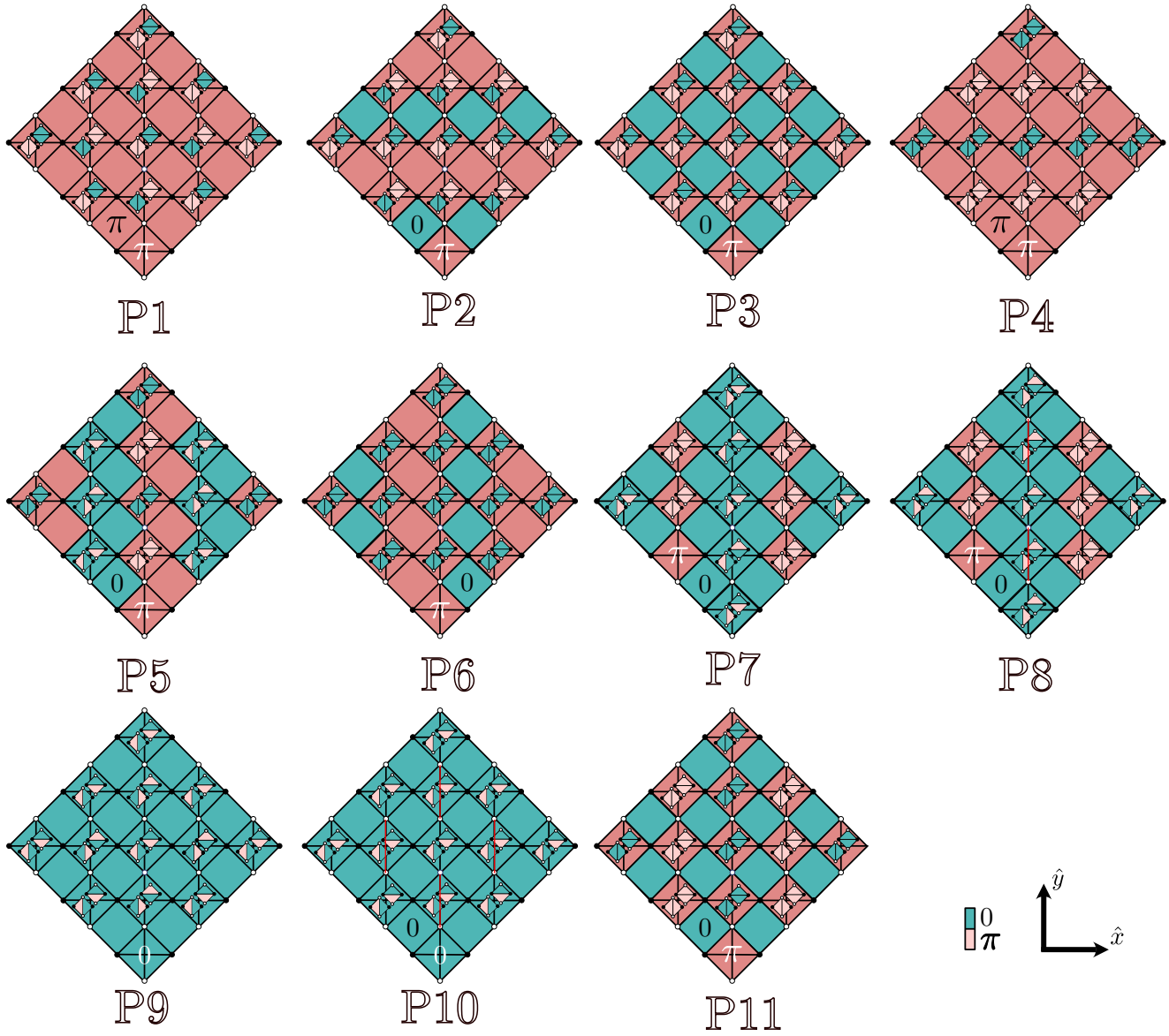


FIG. 8. Schematics of flux configurations found in the extended phase in Fig. 7(a). Elementary plaquettes (empty and crossed squares, and triangles inside the latter) are colored according to their gauge flux values: 0 (green) or π (red). See the discussion in Appendix D for more details about each phase. The red bonds in phase P10 (P8) represent the necessary excitations A [see Fig. 3(a)] to connect this phase to P9 (P7).

Rather than introducing new nomenclature for these additional phases, we summarize their flux configurations and highlight their similarities to the phases shown in Fig. 2(b) as follows:

(i) P1: Similar to the OSSL phase, with orbital antiferromagnetic stripes now present along both the $\hat{x}$ and $\hat{y}$ directions. The flux configuration is invariant under the combined operation $\Theta \times \mathcal{T}_{x,y}$, where $\mathcal{T}_{x,y}$ denotes translation by one unit cell along the x and y directions.

(ii) P2: Orbital (A)FM stripes running along the $\hat{y}$ direction, with staggered π and 0 flux stripe patterns along $(\hat{y})\hat{x}$ on the $\diamondsuit$ plaquettes, and π flux on the $\boxplus$ plaquettes.

(iii) P3: Orbital textures arranged as in the OAMSL (d-wave structure), with a checkerboard pattern of 0 and π fluxes on the $\diamondsuit$ and $\boxplus$ plaquettes, similar to the CSL-II flux configuration. The flux configuration is invariant under the combined operation $\Theta \times C_{4z}$.

(iv) P4: Orbital stripes staggered along the $\hat{y}$ direction with a uniform π flux over the square $\boxplus$ and $\diamondsuit$ plaquettes. The flux configuration is invariant under the combined symmetry $\Theta \times \mathcal{T}_y$.

(v) P5: The flux configuration breaks $\Theta, \mathcal{T}, \sigma_d$ and does not exhibit a simple stripe or checkerboard structure, indicating a more complex orbital ordering, which could be related to this phase appearing at the border of phases CSL-II, P4, and P3 in the extended phase diagram.

(vi) P6: Uniform orbital textures (π flux), with staggered π and 0 flux stripes patterns along $\hat{y}$ on the $\diamondsuit$, and π flux on the $\boxplus$ plaquettes.

(vii) P7: A complex phase with alternating orbital textures $(+,-,+,-) \to (-,+,-,+)$ along the $\hat{y}$ direction and uniform stripes $(-,-,-,-)$ along the $\hat{x}$ direction. The $\diamondsuit$ plaquettes host 0 flux, while the $\boxplus$ have a stripes of alternating 0 and π fluxes along the $\hat{x}$ direction.

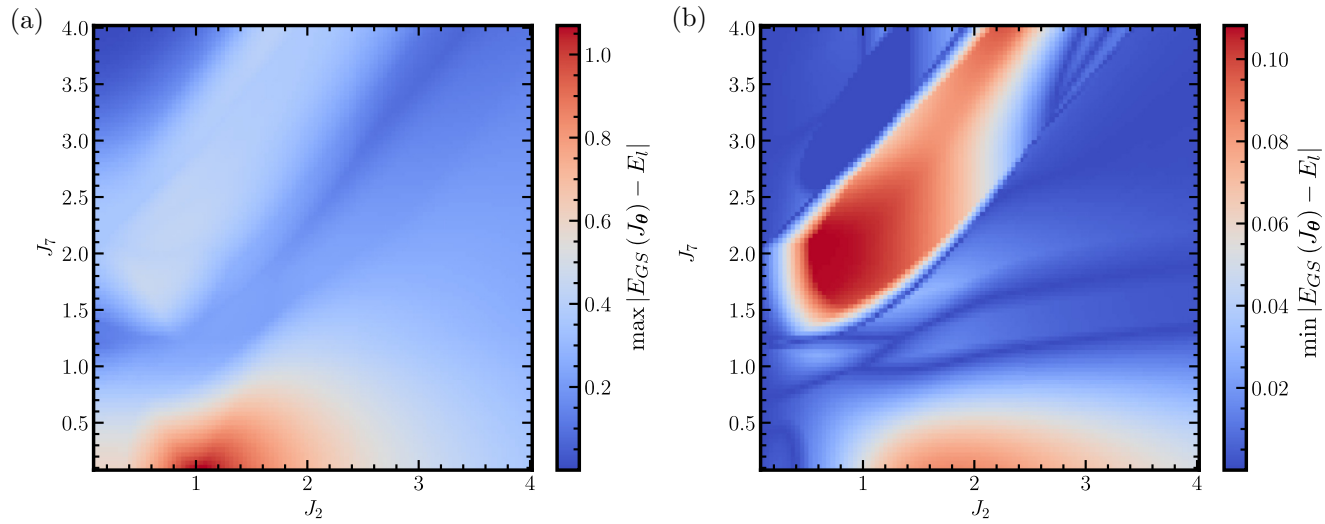


FIG. 9. Maximum (a) and minimum (b) energy differences between the ground state at each $J_{\{2,7\}}$, for $J_2' = J_2$ and $J_1' = J_1 = 1$, and the remaining energies E_l corresponding to each phase in Fig. 7(a).

(viii) P8: Same square and orbital flux pattern as in P7 apart from the fluxes influenced by a flip of the indicated red bonds.

(ix) P9: Uniform 0 flux on all square plaquettes, accompanied by an alternating pattern of $(+,-,+,-) \rightarrow (-,+,-,+)$ on the orbital textures along both directions. The flux configuration is invariant under the combined operation $\Theta \times \mathcal{T}_{x,y}$.

(x) P10: Same square and orbital flux pattern as in P9 apart from the fluxes influenced by a flip of the indicated red bonds, i.e., instead of the alternating pattern, orbital textures have a fixed $(+,-,+,-)$ structure. The flux configuration is invariant under the combined operation $\Theta \times \sigma_d$. Furthermore, the orbital flux structure has a p-wave structure.

(xi) P11: Same square flux patterns as in P3 and the CSL-II. Additionally, hosts staggered orbital stripes of uniform fluxes along the $\hat{y}$ direction. The flux configuration is invariant under the combined operation $\Theta \times \mathcal{T}_x$.

By computing the difference between the ground-state energy E_{GS} at each J_θ and the energies E_l of the remaining phases ($l = 1, \ldots, 15$), we can identify the energy boundaries between phases. In particular, the maximum of this energy difference [Fig. 9(a)] reveals regions where the phases are energetically close, with two such regions highlighted in red in Fig. 7(a), indicating potential degeneracies. Taking instead the minimum of this quantity [Fig. 9(b)] allows us to identify the energetically nearest competing phase.

For example, phases P9 and P10, as well as P8 and P7, are very close in energy, which can be understood from their gauge-flux configurations. As shown in Fig. 8, the red bonds in phases P10 (P8) indicate the bond flips required to reach phases P9 (P7).

All phases appear to be gapless, within the 100×100 momentum-grid resolution used in our simulations, except for the CSL-I and CSL-II phases, which become clearly gapped in certain regions of the phase diagram [Fig. 7(c)]. The degeneracy at the boundary between the CSL-II and the OAMSL phase is also reflected in the vison spectrum (see Fig. 10), where all excitations exhibit a small gap relative to the ground-state energy.

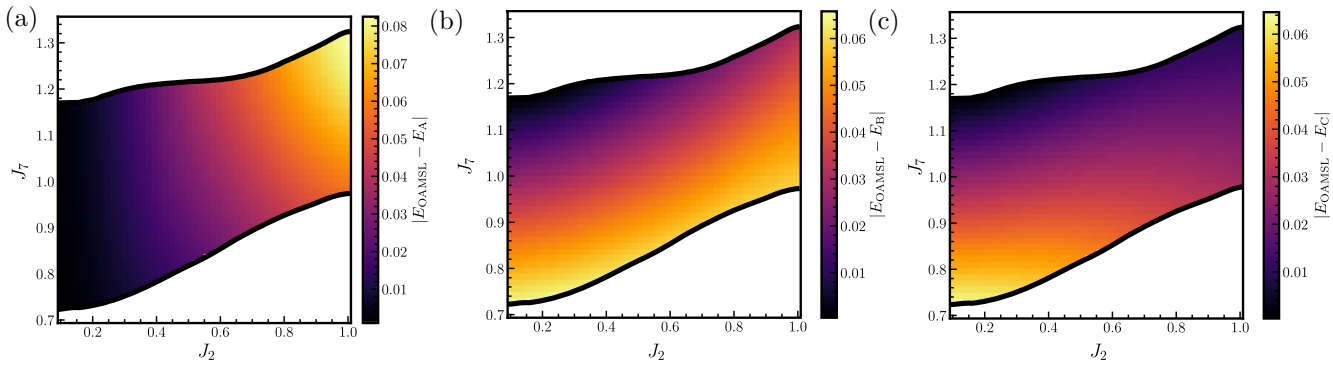


FIG. 10. Energy distribution of the possible excitations for the OAMSL in the spin-$\frac{7}{2}$ model (see Fig. 3): the nontopological excitation A (a), visons B (b) and C (c) as a function of J_2 and J_7 for $J_2' = J_2$ and $J_1' = J_1 = 1$. The color bar indicates the energy difference from each excitation (X) to the OAMSL in $|E_{\mathrm{OAMSL}} - E_{\mathrm{X}}|$.

[1] L. Šmejkal, J. Sinova, and T. Jungwirth, Emerging research landscape of altermagnetism, Phys. Rev. X **12**, 040501 (2022).

[2] T. Jungwirth, R. M. Fernandes, E. Fradkin, A. H. MacDonald, J. Sinova, and L. Šmejkal, Altermagnetism: An unconventional spin-ordered phase of matter, Newton **1**, 100162 (2025).

[3] Z. Liu, H. Hu, and X.-J. Liu, Altermagnetism and superconductivity: A short historical review, Rep. Prog. Phys. **89**, 094501 (2026).

[4] L. Savary and L. Balents, Quantum spin liquids: A review, Rep. Prog. Phys. **80**, 016502 (2017).

[5] Y. Zhou, K. Kanoda, and T.-K. Ng, Quantum spin liquid states, Rev. Mod. Phys. **89**, 025003 (2017).

[6] J. A. Sobral, S. Mandal, and M. S. Scheurer, Fractionalized altermagnets: From neighboring and altermagnetic spin liquids to spin-symmetric band splitting, Phys. Rev. Res. **7**, 023152 (2025).

[7] A. Vijayvargia, E. Day-Roberts, A. S. Botana, and O. Erten, Altermagnets with topological order in Kitaev bilayers, Phys. Rev. Lett. **135**, 166701 (2025).

[8] A. Neehus, A. Rosch, J. Knolle, and Urban F. P. Seifert, Projectively implemented altermagnetism in an exactly solvable quantum spin liquid, Phys. Rev. Lett. **135**, 256504 (2025).

[9] Y. Yu, H. G. Suh, M. Roig, and D. F. Agterberg, Altermagnetism from coincident Van Hove singularities: Application to κ-Cl, Nat. Commun. **16**, 2950 (2025).

[10] L. V. Pupim and M. S. Scheurer, Adatom engineering magnetic order in superconductors: Applications to altermagnetic superconductivity, Phys. Rev. Lett. **134**, 146001 (2025).

[11] A. R. Chakraborty, F. Yang, T. Birol, and R. M. Fernandes, Orbital altermagnetism on the kagome lattice and possible application to AV_3Sb_5, Phys. Rev. B **113**, 214431 (2026).

[12] M. Pan, F. Liu, and H. Huang, Orbital altermagnetism in two dimensions, Phys. Rev. Lett. **137**, 016702 (2026).

[13] A. Kitaev, Anyons in an exactly solved model and beyond, Ann. Phys. **321**, 2 (2006).

[14] A. Vijayvargia, E. M. Nica, R. Moessner, Y.-M. Lu, and O. Erten, Magnetic fragmentation and fractionalized Goldstone modes in a bilayer quantum spin liquid, Phys. Rev. Res. **5**, L022062 (2023).

[15] M. E. Brooks-Bartlett, S. T. Banks, L. D. C. Jaubert, A. Harman-Clarke, and P. C. W. Holdsworth, Magnetic-moment fragmentation and monopole crystallization, Phys. Rev. X **4**, 011007 (2014).

[16] S. Petit, E. Lhotel, B. Canals, M. Ciomaga Hatnean, J. Ollivier, H. Mutka, E. Ressouche, A. R. Wildes, M. R. Lees, and G. Balakrishnan, Observation of magnetic fragmentation in spin ice, Nat. Phys. **12**, 746 (2016).

[17] C. Nayak, Density-wave states of nonzero angular momentum, Phys. Rev. B **62**, 4880 (2000).

[18] T. Senthil, M. Vojta, and S. Sachdev, Weak magnetism and non-Fermi liquids near heavy-fermion critical points, Phys. Rev. B **69**, 035111 (2004).

[19] P. Ghaemi and T. Senthil, Néel order, quantum spin liquids, and quantum criticality in two dimensions, Phys. Rev. B **73**, 054415 (2006).

[20] X.-G. Wen, Quantum orders and symmetric spin liquids, Phys. Rev. B **65**, 165113 (2002).

[21] H. Yao, S.-C. Zhang, and S. A. Kivelson, Algebraic spin liquid in an exactly solvable spin model, Phys. Rev. Lett. **102**, 217202 (2009).

[22] H. Yao and S. A. Kivelson, Exact chiral spin liquid with non-Abelian anyons, Phys. Rev. Lett. **99**, 247203 (2007).

[23] V. Chua, H. Yao, and G. A. Fiete, Exact chiral spin liquid with stable spin Fermi surface on the kagome lattice, Phys. Rev. B **83**, 180412(R) (2011).

[24] E. Demler and S.-C. Zhang, Non-Abelian holonomy of BCS and SDW quasiparticles, Ann. Phys. **271**, 83 (1999).

[25] S. Murakami, N. Nagaosa, and S.-C. Zhang, SU(2) non-Abelian holonomy and dissipationless spin current in semiconductors, Phys. Rev. B **69**, 235206 (2004).

[26] F. L. Pedrocchi, S. Chesi, and D. Loss, Physical solutions of the Kitaev honeycomb model, Phys. Rev. B **84**, 165414 (2011).

[27] F. Zschocke and M. Vojta, Physical states and finite-size effects in Kitaev's honeycomb model: Bond disorder, spin excitations, and NMR line shape, Phys. Rev. B **92**, 014403 (2015).

[28] E. H. Lieb, Two theorems on the Hubbard model, Phys. Rev. Lett. **62**, 1201 (1989).

[29] S. Banerjee and M. S. Scheurer, Altermagnetic superconducting diode effect, Phys. Rev. B **110**, 024503 (2024).

[30] R. M. Fernandes, V. S. de Carvalho, T. Birol, and R. G. Pereira, Topological transition from nodal to nodeless Zeeman splitting in altermagnets, Phys. Rev. B **109**, 024404 (2024).

[31] M. O. Takahashi, W.-H. Kao, S. Fujimoto, and N. B. Perkins, Impurity quadrupole moments as local probes of flux sectors in the Kitaev spin liquid, arXiv:2603.23145.

[32] S.-S. Zhang, Z. Wang, G. B. Halász, and C. D. Batista, Vison crystals in an extended Kitaev model on the honeycomb lattice, Phys. Rev. Lett. **123**, 057201 (2019).

[33] D. Takikawa and S. Fujimoto, Topological phase transition to Abelian anyon phases due to off-diagonal exchange interaction in the Kitaev spin liquid state, Phys. Rev. B **102**, 174414 (2020).

[34] Y.-H. Chen, B.-Z. Wang, T.-F. J. Poon, X.-C. Zhou, Z.-X. Liu, and X.-J. Liu, Proposal for realization and detection of Kitaev quantum spin liquid with Rydberg atoms, Phys. Rev. Res. **6**, L042054 (2024).